

Ultrahigh energy storage density in lead-free antiferroelectric rare-earth-substituted bismuth ferrite

Yehui Zhang¹, Laurent Bellaiche², and Bin Xu^{1,*}

¹*Institute of Theoretical and Applied Physics, Jiangsu Key Laboratory of Thin Films, School of Physical Science and Technology, Soochow University, Suzhou 215006, China*

²*Physics Department and Institute for Nanoscience and Engineering, University of Arkansas, Fayetteville, Arkansas 72701, USA*



(Received 22 February 2022; accepted 3 May 2022; published 20 May 2022)

Dielectric capacitors hold an enormous advantage for energy storage that requires a fast charging/discharging rate; but relatively low energy capacity is a key limitation for conventional dielectric materials. Recently, design strategies by tuning the ferroelectric BiFeO₃ (BFO) to an antiferroelectric or relaxor have shown great promise, especially owing to the large polarization at high electric field. Here, using a first-principles-based method, it is predicted that rare-earth substitution of varied elements and composition can systematically tune the stability of the antiferroelectric phase, leading to further enhanced energy densities and high efficiencies, for instance, reaching 239 J cm⁻³ in thulium substituted BFO and generally beyond 80%, respectively. The storage performance is further interpreted based on a simple model, pointing to the importance of transition fields, polarization of the ferroelectric state, and dielectric constant.

DOI: [10.1103/PhysRevMaterials.6.L051401](https://doi.org/10.1103/PhysRevMaterials.6.L051401)

Electrostatic dielectric capacitors are capable of storing electric energies by displacing electric dipoles with an applied electric field or voltage. They are famed for their ultrahigh charging-discharging rate and stability, making them very promising as indispensable components in electronic devices and power systems for effective management of fluctuating energy sources [1,2]. Despite their high power density, energy densities based on conventional dielectric materials are generally low (a few J cm⁻³), which have greatly hindered their wide applications. The usable energy density is the integrated area of the discharging P - E curve, defined as $W = \int_{P_r}^{P_m} E dP$, where P_r and P_m are the remnant and maximum polarization, respectively. To obtain a large energy density, it is required to have simultaneously small P_r , large P_m , and large breakdown strength E_b . To have a high efficiency, defined as $\eta = W/(W + L)$, where L is the dissipated energy density enclosed by the hysteresis loop, a relatively small hysteresis is desirable.

Antiferroelectrics (AFE), characterized by antipolar internal displacements in a unit cell and exhibiting a double P - E hysteresis loop, hold great promise for energy storage since they can have small P_r in the AFE state and large P_m in the ferroelectric (FE) state. The prototype AFE PbZrO₃ suffers from a relatively low E_b , yielding an energy density of 7.4, 12.2, and 12.5 J cm⁻³ for (001), (110), and (111) films on SrTiO₃ substrate at 700 kV cm⁻¹ [3], and many efforts have been devoted to improve the energy density via doping, pushing W in PZO-based materials to 85 J cm⁻³ [4]. Other AFE or relaxor FEs have also been considered, for instance, materials with BiFeO₃ (BFO) as a major component, in which W values can reach as high as 152 J cm⁻³ [5–7]. Furthermore, AFE neodymium substituted BFO was

predicted to potentially yield even higher energy density with good efficiency [8], as the AFE $Pnma$ phase becomes the ground state with a relatively low amount of substitution [9,10]. The increasing stability of the $Pnma$ phase over the $R3c$ phase is due to the energy gain from a trilinear coupling among the antiphase in-plane octahedral tilting (ω_R), in-phase out-of-plane tilting (ω_M), and the antipolar displacement (X) of the form $\omega_R \omega_M X$, with an increasing amount of rare-earth substitution of Bi atoms [Fig. 1(a)] [11–13]. Such a designing strategy can be naturally extended to substitution with other rare-earth elements which have different ionic radiuses that can further modify the storage performance. Interestingly, a universal behavior was proposed for rare-earth substituted BFO [Bi_{1-x}R_xFeO₃ (BRFO)] [9], in which the FE phase transition and the P - E loop is found to be independent of the rare-earth dopant species, provided that the average ionic radius of A -site cations is the same. Hence one may expect that storage performance of other BRFO can be deduced from (Bi,Nd)FeO₃; however, its validity is not fully known as it was only verified for $x < 0.3$ with rare-earth elements of Sm, Gd, and Dy. Furthermore, for high compositions, some BRFO with small R cannot be equivalently represented by other BRFO with large R . For instance, (Bi,Tm)FeO₃ with $x=0.35$ and (Bi,Nd)FeO₃ with $x=1.0$ have the same average A -site ionic radius. Consequently, (Bi,Tm)FeO₃ systems with x larger than 0.35 do not have any equivalent (Bi,Nd)FeO₃ compounds, and direct investigation of them is indispensable.

In this Letter, we report a systematic study of the energy storage properties of BRFO at room temperature with R being La, Nd, Sm, Gd, Dy, and Tm that covers a wide range of rare-earth elements with decreasing ionic radius. Different compositions and electric field directions are studied for each BRFO, and these three factors (including the variation of R) show significant influence to the energy density and efficiency. The full mapping of the storage performance is predicted,

*binxu19@suda.edu.cn

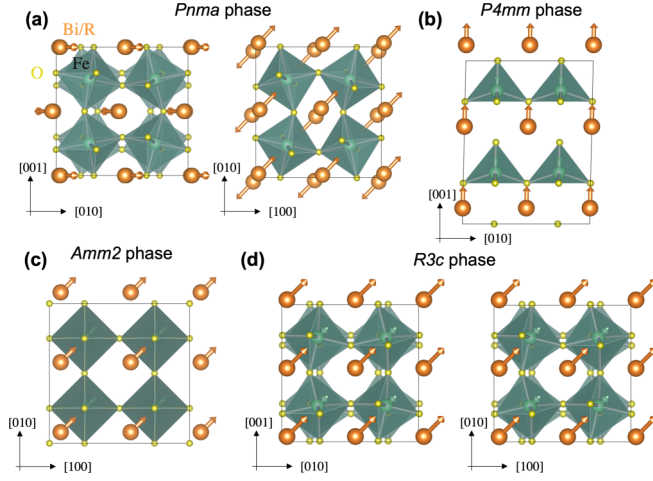


FIG. 1. Structures of $\text{Bi}_{1-x}\text{R}_x\text{FeO}_3$ under zero and applied electric field. (a) The antiferroelectric orthorhombic $Pnma$ phase, characterized by the antipolar distortions along the pseudocubic [110] direction, and the $a^-a^-c^+$ octahedral tilting pattern. (b) The ferroelectric tetragonal $P4mm$ phase, characterized by the polarization along the [001] direction with no octahedral tiltings. (c) The ferroelectric orthorhombic $Amm2$ phase, characterized by the polarization along the [110] direction with no octahedral tiltings. (d) The ferroelectric rhombohedral $R3c$ phase, characterized by the polarization and $a^-a^-a^-$ tiltings along the [111] direction. The arrows denote atomic displacements.

and the most promising candidates are reported. A detailed analysis of the contributing factors is also presented.

The finite-temperature P - E curves of BRFO are simulated via Monte Carlo (MC) simulations based on an effective Hamiltonian approach [13]. The solid solutions are simulated by $12 \times 12 \times 12$ supercells (corresponding to 8640 atoms) with randomly distributed Bi and R atoms. To ensure convergence, for each electric field, we run 20 000 MC sweeps for equilibration and additional 20 000 MC sweeps to obtain the statistical thermal averages.

The effective Hamiltonian of BRFO includes four types of degrees of freedom: (1) the local modes $\{\mathbf{u}_i\}$ centered on the A sites (i.e., on Bi or R ions), which are directly related to the local electric dipoles [14,15]; (2) the homogeneous $\{\eta_H\}$ and inhomogeneous $\{\eta_I\}$ strain tensors [14,15]; (3) the pseudovectors $\{\boldsymbol{\omega}_i\}$ that characterize the oxygen octahedral tiltings [16]; and (4) the magnetic moments $\{\mathbf{m}_i\}$ of the Fe ions. (In all cases, the subscript i labels unit cells in our simulated supercell.) To quantify the doping effect, a local quantity $\eta_{\text{loc}}(i)$ centered on the Fe-site i is also introduced as $\eta_{\text{loc}}(i) = \frac{\delta R_{\text{ionic}}}{8} \sum_j \sigma_j$, where σ_j (0 or 1) accounts for the presence of Bi or R ions at the A site j and the sum over j runs over the eight nearest neighbors of Fe-site i and where δR_{ionic} represents the relative difference in ionic radius between R and Bi ions. $\eta_{\text{loc}}(i)$ is thus different from zero if at least one of these eight A sites are occupied by the R ions, while it is zero for pure BFO.

In this effective Hamiltonian, the total energy can be expressed as a sum of two terms,

$$E_{\text{tot}} = E_{\text{BFO}}(\{\mathbf{u}_i\}, \{\eta_H\}, \{\eta_I\}, \{\boldsymbol{\omega}_i\}, \{\mathbf{m}_i\}) + E_{\text{alloy}}(\{\mathbf{u}_i\}, \{\boldsymbol{\omega}_i\}, \{\mathbf{m}_i\}, \{\eta_{\text{loc}}\}), \quad (1)$$

where E_{BFO} is the effective Hamiltonian of pure BFO [17–20] and E_{alloy} characterizes the effect of substituting Bi by R ions. The parameters of the Hamiltonian are obtained by performing first-principles calculations, and details about this method with Nd substitution can be found in Ref. [13] and references therein. For substitution with other rare-earth ions, we adopt a similar approach for which the coefficient of the harmonic energy of the local mode is allowed to vary to reproduce the experimental Curie temperature T_C of BRFO solid solutions, when $R=\text{La}$, Nd, Sm, and Gd [10]. For Dy and Tm, their T_C (experimental values not available) are obtained by linear extrapolation (see Supplemental Material (SM) Fig. S1 [21]). Under an applied electric field, an additional term $-\sum_i \mathbf{p}_i \cdot \mathbf{E}_i$ is incorporated, where the local electric dipoles \mathbf{p}_i are computed from the local modes $\{\mathbf{u}_i\}$ and effective charges Z_i^* .

Furthermore, the theoretical critical field is typically much larger than that in experiments, as explained by Landauer's paradox [22]. Numerically, an approximate factor of 23 was found for $\text{Bi}_{1-x}\text{Nd}_x\text{FeO}_3$ by fitting to the experimental P - E loop, as adopted in Ref. [8]. In this Letter, we estimate the scale factor of $\text{Bi}_{1-x}\text{R}_x\text{FeO}_3$ with $R=\text{Sm}$, Gd, Dy, or Tm, by taking $\text{Bi}_{0.9}\text{Nd}_{0.1}\text{FeO}_3$ as a reference and considering the universal behavior proposed in Ref. [9]. The corresponding composition to 10% Nd that yields the same average A -site ionic radius is 6.7%, 5.2%, 4.3%, and 3.5% for Sm, Gd, Dy, and Tm substituted BFO, respectively, and the respective scale factor is found to be 27, 28, 27, and 19 (see SM Fig. S2 [21]). Note that for $\text{Bi}_{1-x}\text{La}_x\text{FeO}_3$, since the ionic radius of La^{3+} is almost identical to that of Bi^{3+} , which cannot be described by the universal law; we find a factor of 26 by direct comparison with the experimental P - E curve of $\text{Bi}_{0.85}\text{La}_{0.15}\text{FeO}_3$ on a (110) substrate [23], i.e., under [110] electric field (see SM Fig. S3 [21]). Also note that the scale factor for each BRFO is assumed to be independent of x , which is a reasonable approximation as it originates from the extrinsic effects in experimental samples, such as crystal inhomogeneities or weak spots, including lattice defects, surface layers, or small residual nuclei, provided that the samples have similar quality (see SM Fig. S4 [21]).

From $(\text{Bi},\text{La})\text{FeO}_3$ to $(\text{Bi},\text{Tm})\text{FeO}_3$, we calculate the P - E loops using the above-mentioned first-principles-based effective Hamiltonian approach. The maximum applied E field is 4.37 MV cm^{-1} , which is estimated to be the intrinsic breakdown field (E_b) according to an empirical relation and the experimental band gap of pure BFO [24,25]. Such magnitude of the field was demonstrated to be feasible in BFO-based thin films [6,7,26]. By increasing the atomic number of the rare-earth element, the hysteresis loops change systematically (see SM Figs. S5–S10 [21]), and we show here the case of $(\text{Bi},\text{Sm})\text{FeO}_3$ as a representative example.

In Fig. 2, we depict the P - E curves at various compositions under four different electric-field (E -field) directions. Similar to $(\text{Bi},\text{Nd})\text{FeO}_3$ [8], starting from the same initial $Pnma$ phase that has an antipolar distortion in the [110] direction, $(\text{Bi},\text{Sm})\text{FeO}_3$ (and other BRFO) transforms to different FE phases under different E directions, i.e., $P4mm$ (T phase, Fig. 1(b)) for [001] and [100] fields, $Amm2$ (O phase, Fig. 1(c)) for [110] field, and $R3c$ (R phase, Fig. 1(d)) for [111] field. More details about the AFE and FE structures

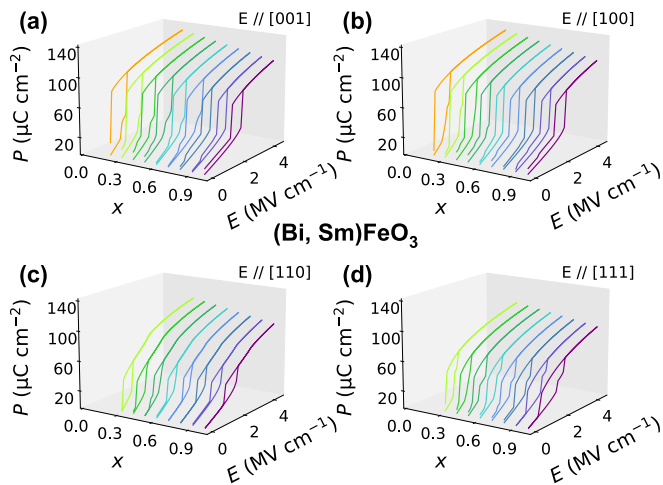


FIG. 2. Calculated unipolar P - E hysteresis curves of $\text{Bi}_{1-x}\text{Sm}_x\text{FeO}_3$ solid solutions for compositions ranging between 0.2 and 1.0 under four different electric field orientations, viz., (a) [001], (b) [100], (c) [110], (d) [111]. The displayed polarization is the projected component of the total polarization along the direction of the applied E field. The initial state is the antiferroelectric $Pnma$ phase. Only curves with approximately recoverable behaviors are shown.

can be found in Ref. [8]. Since the O and R phases are more stable than the T phase under zero field, the AFE state that is recoverable during the discharging process for [001] (or [100]) field may not be similar for [110] and [111] fields at low composition, and only cases with approximately recoverable AFE states are shown [27]. Also, P - E loops of additional charging/discharging cycles are found to reproduce the loop of the first cycle reported here. It is worth mentioning that, as verified in Ref. [8], the computed polarization and critical field of the R phase $(\text{Bi,Nd})\text{FeO}_3$ are in good agreement with experiments, implying that the predictions here can be taken semiquantitatively, especially also considering the uncertainties in measurements.

In $(\text{Bi,L a})\text{FeO}_3$ (see SM Fig. S5 [21]), due to the closeness of ionic radius between La and Bi, i.e., 1.16 versus 1.17 Å [28], the $R3c$ phase remains the ground state for low La compositions. In other words, the AFE phase is not recovered during the discharging process in those cases, and the system becomes FE in the following cycles; therefore, they are not suitable for energy storage due to the much reduced energy densities. Approximately double hysteresis loops can only be achieved for $x \geq 0.5$ under [001] or [100] field and for $x \geq 0.7$ under [110] or [111] field. Note that increasing x has two general effects (for all BRFO): (1) the critical fields for the AFE-to-FE (E_{up}) and FE-to-AFE (E_{down}) transitions increase and (2) polarization of the FE state decreases. Clearly, these two behaviors affect the energy storage properties in an opposite way: in general large polarization, a high FE-to-AFE transition and small hysteresis is desired.

As we increase the atomic number of the rare-earth element (see SM Fig. S11 [21]), the critical x for recovering the $Pnma$ phase decreases, i.e., double loops are available for lower x ; however, the AFE-to-FE transition shifts to higher critical

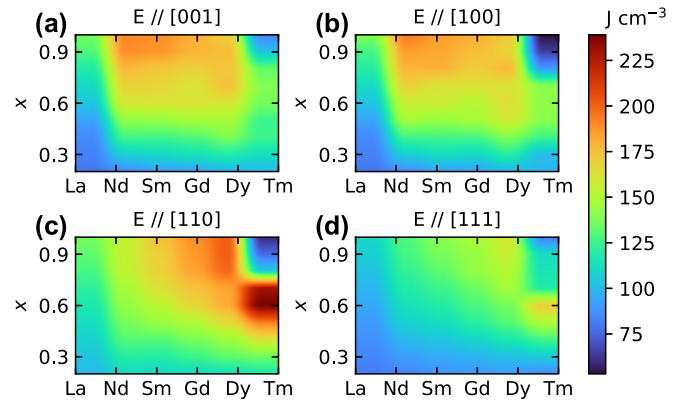


FIG. 3. The calculated energy densities of $\text{Bi}_{1-x}\text{R}_x\text{FeO}_3$ ($R=\text{La, Nd, Sm, Gd, Dy, or Tm}$) solid solutions at various compositions ($x=0.2-1.0$) under four different electric field orientations, viz., (a) [001]. (b) [100]. (c) [110]. (d) [111], with the maximum applied E field (E_{max}) being 4.37 MV cm^{-1} .

field at the same time (see SM Fig. S12 [21]). In particular, for small rare-earth element $(\text{Bi,Tm})\text{FeO}_3$ with high composition (see SM Fig. S10 [21]), the AFE-to-FE transition may not occur even at the breakdown field or it transforms only to an intermediate phase with much smaller polarization than the FE state. For those cases, the corresponding energy density would deteriorate significantly (as we will show next), which is not suitable for energy storage. Further, the hysteresis is found to shrink with increasing x for rare-earth elements before Gd, but it enlarges for elements after Gd. For the same x , the hysteresis is also found to enlarge with smaller-size rare-earth substitution. This implies that the efficiency strongly depend on the composition x and the R element.

With the computed P - E curves, we are allowed to compute the energy storage density and efficiency for each BRFO with changing composition under four field directions. To best illustrate the variations, we plot W as heat maps, as shown in Fig. 3. Let us first focus on the qualitatively similar [001] and [100] fields. In general, each BRFO exhibits monotonously increasing W with higher x , except for rare earths with a radius smaller than Dy, in which the AFE-to-FE transition may not occur at the breakdown field. On the other hand, comparing different BRFO, La and Tm substitution have apparently smaller W due to their too large or too small ionic radii, whereas between Nd and Dy the behaviors are very similar. For these four cases, the highest W is about 190 J cm^{-3} given by $x = 1.0$, i.e., pure RFeO_3 . If the field is along [110], the increasing trend with respect to x for each BRFO remains except $(\text{Bi,Tm})\text{FeO}_3$ at $x > 0.7$, but changing from La toward Tm shows a different behavior, i.e., W generally increases and can reach as high as 239 J cm^{-3} from $(\text{Bi,Tm})\text{FeO}_3$ at $x=0.6$. The field along [111] has a similar trend as that of the [110] field, but the magnitude of W is significantly reduced.

The calculated efficiencies η are shown in Fig. 4. The behaviors with respect to x and rare-earth elements are apparently different from that of W . By ignoring La at low composition and Tm (or Dy) at high compositions where the double hysteresis loops are absent, increasing x yields

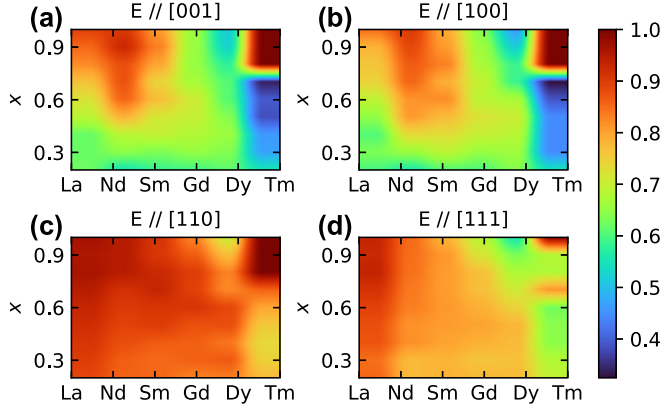


FIG. 4. The calculated efficiencies of $\text{Bi}_{1-x}\text{R}_x\text{FeO}_3$ ($R=\text{La}, \text{Nd}, \text{Sm}, \text{Gd}, \text{Dy}, \text{or Tm}$) solid solutions at various compositions ($x=0.2-1.0$) under four different electric field orientations, viz., (a) [001], (b) [100], (c) [110], (d) [111], with the maximum applied E -field (E_{max}) being 4.37 MV cm^{-1} .

higher η for fields along [001] or [100] direction, while the x dependence is insensitive for [110] and [111] fields. And in contrast to W , η decreases with the increase of atomic number of the rare earth; which hence suggests that a balance between W and η needs to be considered when choosing the rare-earth element and composition. Regarding the field directions, which in reality rely on the crystallographic orientation of the substrate, both W and η indicate that the [111] field has an overall inferior performance than that of the [110] field, while [001] and [100] fields provide very similar results.

In Table I, we list the highest W achieved for each BRFO solid solution and the corresponding η , in comparison with experimental values of other dielectric films, including FEs [4], AFEs [29,30], relaxors [6], and superparaelectric relaxors [7]. Changing from La to Tm, the general trend is that the highest W increases (from 136 to 239 J cm^{-3}) while the corresponding η decreases (from 89% to 80%). The predicted W of these representative BRFO cases are among the best reported values or even better, and the relatively low efficiency of $(\text{Bi},\text{Tm})\text{FeO}_3$ at $x=0.6$ and $E//[110]$ is still comparable to the

TABLE I. Comparison of the energy storage performance of BRFO solid solutions with that of other best-available dielectric films.

	W (J cm^{-3})	η (%)	E_b (MV cm^{-1})
PLZST [29]	56	~44	3.7
PLZT [4]	85	65	4.5
$\text{Hf}_{0.3}\text{Zr}_{0.7}\text{O}_2$ [30]	46	51	4.5
0.25BFO–0.75STO [5]	70	68	4.5
0.25BFO–0.3BTO–0.45STO [6]	112	80	4.9
0.3BSFO–0.7BTO [7]	152	~78	5.2
$(\text{Bi},\text{La})\text{FeO}_3$ ($x=1.0, E//[001]$)	136	89	4.37
$(\text{Bi},\text{Nd})\text{FeO}_3$ ($x=1.0, E//[001]$)	190	90	4.37
$(\text{Bi},\text{Sm})\text{FeO}_3$ ($x=1.0, E//[001]$)	188	81	4.37
$(\text{Bi},\text{Gd})\text{FeO}_3$ ($x=1.0, E//[110]$)	188	83	4.37
$(\text{Bi},\text{Dy})\text{FeO}_3$ ($x=0.9, E//[110]$)	201	77	4.37
$(\text{Bi},\text{Tm})\text{FeO}_3$ ($x=0.6, E//[110]$)	239	80	4.37

best-available dielectric thin films. Note that the listed cases have different optimal compositions and E -field directions. For instance, the optimal x decreases as E changes from [001] (or [100]) to [110], which means these factors can effectively influence the energy storage performance.

To understand the origin of the aforementioned trends, we can express W and η based on a simplified model [8], assuming the same constant dielectric constant of the AFE and FE state, and abrupt transitions between the two states, as sketched in Fig. 5(a),

$$W = P_{\text{FE}}^0 E_{\text{down}} + \frac{1}{2} \epsilon_0 \chi E_{\text{max}}^2, \quad (2)$$

$$\eta = \frac{P_{\text{FE}}^0 E_{\text{down}} + \frac{1}{2} \epsilon_0 \chi E_{\text{max}}^2}{P_{\text{FE}}^0 E_{\text{up}} + \frac{1}{2} \epsilon_0 \chi E_{\text{max}}^2}, \quad (3)$$

where P_{FE}^0 is the remnant polarization of the FE phase extrapolated to $E = 0$; χ is the dielectric constant; E_{down} , E_{up} , and E_{max} are the FE-to-AFE, AFE-to-FE, and maximum field, respectively. P_{FE}^0 and χ can be extracted by quadratic fitting to the P - E curve of the FE state (the effective Hamiltonian predicts a nonlinear field dependence of χ), in which P decreases gradually with the E field.

This simple model indicates that improving W requires either large P_{FE}^0 , large E_{down} , large χ , high E_b , or ideally all these quantities being large. Assuming approximately the same E_b , W is determined by the sum of two areas, i.e., $P_{\text{FE}}^0 E_{\text{down}}$ and $\frac{1}{2} \epsilon_0 \chi E_b^2$. In $(\text{Bi},\text{La})\text{FeO}_3$, W at $x=1.0$ is similar for [001] and [110] fields (136 versus 137 J cm^{-3}), but the contributions are different: [001] field has larger P_{FE}^0 and E_{down} , and smaller χ ; [110] field has smaller P_{FE}^0 and E_{down} , and larger χ (see SM Figs. S11, S13, and S14 [21]). The difference between E_{up} and E_{down} is smaller under the [110] field than that of the [001] field (see SM Figs. S11 and S14 [21]), contributing to a slightly higher η .

With the change of rare-earth element, E_{down} , P_{FE}^0 , and χ under the [001] field show alike patterns, except that E_{down} maximizes and P_{FE}^0 minimizes around Nd at $x=0.2$, while χ is less sensitive and only slightly favorable for $(\text{Bi},\text{Nd})\text{FeO}_3$. Such compensation explains the similarity of W found in $(\text{Bi},\text{Nd})\text{FeO}_3$, $(\text{Bi},\text{Sm})\text{FeO}_3$, and $(\text{Bi},\text{Gd})\text{FeO}_3$ cases. Further considering that E_{up} increases significantly from $(\text{Bi},\text{La})\text{FeO}_3$ to $(\text{Bi},\text{Tm})\text{FeO}_3$ under the [001] field, η decreases correspondingly. For the [110] field, E_{down} increases from $(\text{Bi},\text{La})\text{FeO}_3$ to $(\text{Bi},\text{Tm})\text{FeO}_3$, P_{FE}^0 and χ are relatively insensitive, contributing to the improving W . E_{up} and E_{down} share similar patterns, but the difference between them slightly increases,

TABLE II. The AFE-to-FE transition fields (E_{up}) of the BRFO solid solutions in Fig. 5(b).

	E_{up} (MV cm^{-1})
$(\text{Bi},\text{La})\text{FeO}_3$ ($x=1.0, E//[001]$)	0.808
$(\text{Bi},\text{Nd})\text{FeO}_3$ ($x=1.0, E//[001]$)	2.217
$(\text{Bi},\text{Sm})\text{FeO}_3$ ($x=1.0, E//[001]$)	2.222
$(\text{Bi},\text{Gd})\text{FeO}_3$ ($x=1.0, E//[110]$)	2.400
$(\text{Bi},\text{Dy})\text{FeO}_3$ ($x=0.9, E//[110]$)	2.667
$(\text{Bi},\text{Tm})\text{FeO}_3$ ($x=0.6, E//[110]$)	3.316

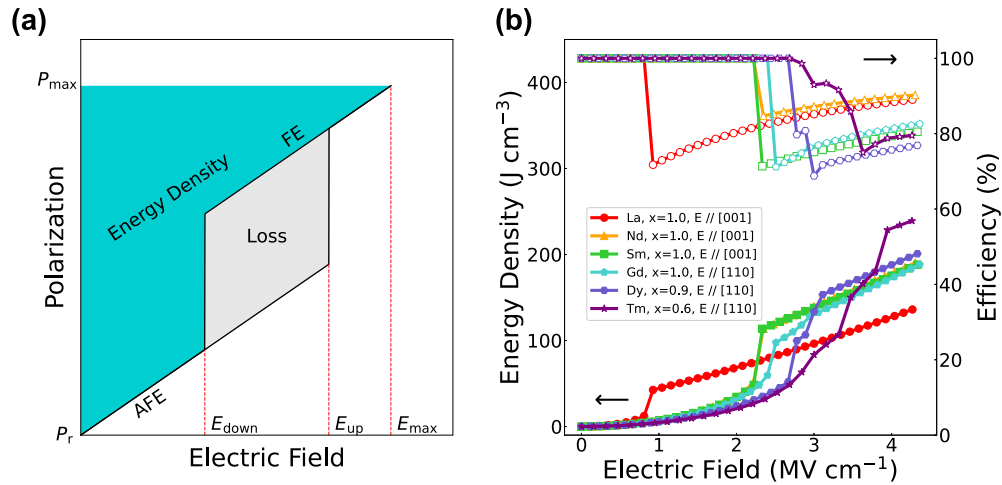


FIG. 5. (a) Schematic unipolar double hysteresis P - E curve of antiferroelectrics. E_{up} and E_{down} are the abrupt AFE-to-FE and FE-to-AFE transition fields, respectively. (b) Calculated energy density and efficiency of representative $\text{Bi}_{1-x}\text{R}_x\text{FeO}_3$ ($R=\text{La, Nd, Sm, Gd, Dy, or Tm}$) solid solutions as a function of electric field.

which explains the slightly decreasing η . While regarding the larger W of Tm at $x=0.6$ and $[110]$ field compared with Nd or Sm at $x=1.0$ and $[001]$ field, it is mainly due to the larger χ since P_{FE}^0 and E_{down} are similar between them.

Finally, we predict the energy density and efficiency of the representative cases (Table I) as a function of electric field up to E_b , as shown in Fig. 5(b). When the field strength is below E_{up} (see Table II), W increases quadratically according to Eq. (2). $(\text{Bi,Tm})\text{FeO}_3$ at $x=0.6$ and $E//[110]$ can reach a remarkable value of $W=239 \text{ J cm}^{-3}$ even before the transition to the FE O phase. And, ideally, η is 100% in these field regimes without domain formations, where the discharging curve overlaps with the charging curve. However, for cases with the occurrence of intermediate phase(s) during the AFE-to-FE transition, e.g., in $(\text{Bi,Nd})\text{FeO}_3$, $(\text{Bi,Dy})\text{FeO}_3$, and $(\text{Bi,Tm})\text{FeO}_3$, a hysteresis loop can form and η drops below 100%.

If the applied field is above E_{up} , the AFE-to-FE transition induces an abrupt increase of W and a concomitant sudden decrease of η . Being able to further increase the maximum field brings monotonous improvement of both W and η . In particular, the increase of W with respect to the electric field is close to linear, i.e., being below the quadratic trend predicted by Eq. (2), due to the decreasing dielectric constant χ (see SM Fig. S14 [21]). On the other hand, the increase of η as a function of E_{max} is below linear and saturates at high field, as the $\frac{1}{2}\epsilon_0\chi E_{\text{max}}^2$ term in Eq. (3) takes increasing proportions. For a fixed field direction, the saturated value of η is found to decrease with the increasing atomic number of R , and the $[110]$ field appears to yield relatively higher efficiency than $[001]$ field due to the smaller hysteresis loop.

In summary, we have systematically studied the energy storage properties of $\text{Bi}_{1-x}\text{R}_x\text{FeO}_3$ solid solutions with rare earth R from La to Tm and composition from 0.2 to 1.0 based on a state-of-the-art effective Hamiltonian approach. Remarkably high-energy densities can be achieved in these relatively simple lead-free compounds, for instance, 239 J cm^{-3} in $(\text{Bi,Tm})\text{FeO}_3$ with $x=0.6$ under an electric field along the $[110]$ direction, thanks to the tunability of the AFE-to-FE and FE-to-AFE transitions, the large polarization in the FE state, and sizable dielectric constant. The efficiencies are also generally above 80% due to the relatively small energy barriers between the AFE and FE phases. The full analysis of the energy storage performance with respect to the controllable variables, including the R element, composition, and the field direction, demonstrates that $\text{Bi}_{1-x}\text{R}_x\text{FeO}_3$ is a rich system that can provide excellent performance with many choices, even with intermediate composition or electric field. In real applications, epitaxial strain is another handle that may further enhance the storage properties. We hope our predictions can soon be actualized in experiments.

This work is supported by the Natural Science Foundation of Jiangsu Province (No. BK20201404), National Natural Science Foundation of China under Grant No. 12074277, the startup fund from Soochow University, and support from Priority Academic Program Development (PAPD) of Jiangsu Higher Education Institutions. L.B. thank the Office of Naval Research for support under Grant No. N00014-21-1-2086, ARO Grant No. W911NF-21-1-0113, and the Vannevar Bush Faculty Fellowship Grant No. N00014-20-1-2834 from the Department of Defense.

- [1] S. A. Sherrill, P. Banerjee, G. W. Rubloff, and S. B. Lee, *Phys. Chem. Chem. Phys.* **13**, 20714 (2011).
 [2] L. C. Haspert, E. Gillette, S. B. Lee, and G. W. Rubloff, *Energy Environ. Sci.* **6**, 2578 (2013).

- [3] J. Ge, PbZrO₃-based antiferroelectric films for energy storage applications, Ph.D. thesis, Université de Valenciennes et du Hainaut-Cambresis, 2015.
 [4] B. Ma, Z. Hu, R. E. Koritala, T. H. Lee, S. E. Dorris, and U. Balachandran, *J. Mater. Sci.: Mater. Electron.* **26**, 9279 (2015).

- [5] H. Pan, J. Ma, J. Ma, Q. Zhang, X. Liu, B. Guan, L. Gu, X. Zhang, Y. J. Zhang, L. Li *et al.*, *Nat. Commun.* **9**, 1813 (2018).
- [6] H. Pan, F. Li, Y. Liu, Q. Zhang, M. Wang, S. Lan, Y. Zheng, J. Ma, L. Gu, Y. Shen *et al.*, *Science* **365**, 578 (2019).
- [7] H. Pan, S. Lan, S. Xu, Q. Zhang, H. Yao, Y. Liu, F. Meng, E. J. Guo, L. Gu, D. Yi *et al.*, *Science* **374**, 100 (2021).
- [8] B. Xu, J. Íñiguez, and L. Bellaiche, *Nat. Commun.* **8**, 15682 (2017).
- [9] D. Kan, L. Pálová, V. Anbusathaiah, C. J. Cheng, S. Fujino, V. Nagarajan, K. M. Rabe, and I. Takeuchi, *Adv. Funct. Mater.* **20**, 1108 (2010).
- [10] S. Karimi, I. Reaney, Y. Han, J. Pokorny, and I. Sterianou, *J. Mater. Sci.* **44**, 5102 (2009).
- [11] L. Bellaiche and J. Íñiguez, *Phys. Rev. B* **88**, 014104 (2013).
- [12] H. J. Zhao, J. Íñiguez, W. Ren, X. M. Chen, and L. Bellaiche, *Phys. Rev. B* **89**, 174101 (2014).
- [13] B. Xu, D. Wang, J. Íñiguez, and L. Bellaiche, *Adv. Funct. Mater.* **25**, 552 (2015).
- [14] W. Zhong, D. Vanderbilt, and K. M. Rabe, *Phys. Rev. Lett.* **73**, 1861 (1994).
- [15] W. Zhong, D. Vanderbilt, and K. M. Rabe, *Phys. Rev. B* **52**, 6301 (1995).
- [16] I. A. Kornev, L. Bellaiche, P.-E. Janolin, B. Dkhil, and E. Suard, *Phys. Rev. Lett.* **97**, 157601 (2006).
- [17] S. Prosandeev, D. Wang, W. Ren, J. Íñiguez, and L. Bellaiche, *Adv. Funct. Mater.* **23**, 234 (2013).
- [18] D. Albrecht, S. Lisenkov, W. Ren, D. Rahmedov, I. A. Kornev, and L. Bellaiche, *Phys. Rev. B* **81**, 140401(R) (2010).
- [19] I. A. Kornev, S. Lisenkov, R. Haumont, B. Dkhil, and L. Bellaiche, *Phys. Rev. Lett.* **99**, 227602 (2007).
- [20] S. Lisenkov, I. A. Kornev, and L. Bellaiche, *Phys. Rev. B* **79**, 012101 (2009).
- [21] See Supplemental Material at <http://link.aps.org/supplemental/10.1103/PhysRevMaterials.6.L051401> for (1) extrapolation of the experimental Curie temperatures, (2) calibration of the theoretical E field, (3) justification of the scale factor, (4) P - E hysteresis curves of all BRFO solid solutions, (5) FE-to-AFE transition fields, (6) AFE-to-FE transition fields, (7) extrapolated remnant polarization, and (8) dielectric susceptibility.
- [22] R. Landauer, *J. Appl. Phys.* **28**, 227 (1957).
- [23] B. Prasad, Y. L. Huang, R. V. Chopdekar, Z. Chen, J. Steffes, S. Das, Q. Li, M. Yang, C.-C. Lin, T. Gosavi *et al.*, *Adv. Mater.* **32**, 2001943 (2020).
- [24] L. M. Wang, in *Proceedings of 25th International Conference on Microelectronics* (IEEE, Piscataway, NJ, 2006), pp. 576–579.
- [25] J. Ihlefeld, N. Podraza, Z. Liu, R. Rai, X. Xu, T. Heeg, Y. Chen, J. Li, R. Collins, J. Musfeldt *et al.*, *Appl. Phys. Lett.* **92**, 142908 (2008).
- [26] P. Chen, R. J. Sichel-Tissot, J. Young Jo, R. T. Smith, S.-H. Baek, W. Saenrang, C.-B. Eom, O. Sakata, E. M. Dufresne, and P. G. Evans, *Appl. Phys. Lett.* **100**, 062906 (2012).
- [27] For unrecoverable cases, the structure returns to a polar phase when discharging to zero field. The polar phase can be the ferroelectric phase or an intermediate complex phase with reduced polarization.
- [28] R. D. Shannon and C. T. Prewitt, *Acta Cryst. B* **25**, 925 (1969).
- [29] X. Hao, Y. Wang, L. Zhang, L. Zhang, and S. An, *Appl. Phys. Lett.* **102**, 163903 (2013).
- [30] M. H. Park, H. J. Kim, Y. J. Kim, T. Moon, K. D. Kim, and C. S. Hwang, *Adv. Energy Mater.* **4**, 1400610 (2014).